ADVANCED FUNCTIONAL MATERIALS
www.afm-journal.de

Highly Efficient Porous Glass Solar Water Evaporator

*Junsheng Liu, Wenqing Ruan, Heting Zhang, Jinbiao Huang, Jiahao Wang, Jianan Fu, Fei Sun, Lixing Zhu, Yangguang Zhan, and Jiang Ma**

The global water crisis, exacerbated by excessive use and pollution, has resulted in energy scarcity and threats. Solar desalination provides a sustainable fix, with researchers developing photothermal materials and designs to improve efficiency and sustainability. Glass materials, with their exceptional chemical stability, are suitable for extreme desalination in acidic and alkaline conditions. In this work, we have developed a porous glass evaporator (PGE) with exceptional water evaporation efficiency, achieved through a novel fabrication method that blends glass powders with soluble salts to create structure with continuous pores. The evaporator's microstructure comprises micrometer-scale pores that form interconnected porous channels, facilitating efficient water transport and preventing salt deposition. Under one sun irradiation, the PGE exhibits superior solar evaporation performance in pure water, achieving a rate of 2.21 kg m^{-2} h^{-1}, with an evaporation efficiency of 98%. In more complex media, such as seawater and methylene blue solution, the PGE also displays excellent evaporation capabilities, reaching rates of 2.08 and 2.47 kg m^{-2} h^{-1}, respectively. Even after sustained alternation between acidic and alkaline treatments, the PGE retains an impressive evaporation rate of over 2.0 kg m^{-2} h^{-1}, coupled with structural robustness, making it a promising candidate for practical applications in extreme environments.

1. Introduction

The over-extraction of freshwater and the burgeoning issue of water pollution due to human activities have escalated water scarcity and energy deficits into paramount challenges imperiling human survival. Statistics show that over one-fifth of the world's population lacks access to adequate water resources, and by 2050, five billion people will face water shortages.[1,2] Moreover, large volumes of industrial wastewater are discharged into oceans, rivers, and lakes, significantly increasing the levels of heavy metal ions and pollutants in water bodies, posing a grave threat to both human health and the natural environment as the ecological cycle unfolds.[3,4] Consequently, addressing the water crisis is an urgent task. As a renewable and clean energy source, solar energy is infinite and has the potential to effectively resolve the energy crisis.[5–7] Earth receives ≈3 × 10^{24} joules of energy from the sun each year. Harvesting just 0.1% of this energy would be sufficient to meet the world's energy needs for an entire year. Therefore, solar water evaporation technology, which utilizes solar energy to extract potable water from seawater and wastewater, offers a promising solution to freshwater scarcity.[5,8,9] This technology requires no additional energy beyond solar energy and does not necessitate the construction of large-scale equipment,[10] making it an increasingly attractive research topic in the scientific community.[11] It holds great potential to become one of the most important solutions to the problem of freshwater scarcity.[12]

An ideal solar steam generation system should adeptly harness solar energy, boasting a high photothermal conversion efficiency.[13–15] Additionally, it must possess exceptional thermal management capabilities, efficient water transport properties, superior salt resistance, and long-term evaporation stability.[16] Photothermal materials represent an indispensable component within solar steam generation systems. Researchers are increasingly utilizing photothermal materials for solar evaporators, such as semiconductors,[17,18] metal nanoparticles,[19–22] carbon-based materials,[23,24] and conjugated polymers. However, the issue of inefficient energy conversion in solar evaporators has been the major focus of research. Some researchers have attempted to enhance the evaporation efficiency by synthesizing 3D macroscopic structures,[25–27] such as honeycomb, lotus and cone array structures, which minimize the reflection of incident light to increase energy input. Furthermore, researchers have explored optimizing water transport by using substrates with hydrophilic and internally interconnected channels as evaporator substrates,[28,29] such as aerogels with an internal porous network that promotes water enhancement through the capillary effect of internally

J. Liu, W. Ruan, H. Zhang, J. Huang, J. Wang, L. Zhu, Y. Zhan, J. Ma
State Key Laboratory of Radio Frequency Heterogeneous Integration
College of Mechatronics and Control Engineering
Shenzhen University
Shenzhen 518060, China
E-mail: majiang@szu.edu.cn

J. Fu
Department of Mechanics and Aerospace Engineering
Southern University of Science and Technology
Shenzhen, Guangdong 518055, China

F. Sun
Department of Materials Science and Engineering
Fujian University of Technology
Fuzhou 350118, China

The ORCID identification number(s) for the author(s) of this article can be found under https://doi.org/10.1002/adfm.202415394

DOI: 10.1002/adfm.202415394

interconnected micro/nanochannels.[8,30] Moreover, as water evaporates during the desalination process, the concentration of salt ions on the surface inevitably increases. The formation of salt crystals will result in a significant reduction in the effective surface area of the evaporator and block water transport pathways. Researchers have designed various structures to mitigate salt crystallization to prevent salt accumulation on the evaporation surface, such as Janus structures that repel salt ions due to their hydrophobic surface and minimize accumulation.[31,32] Similarly, the impact of heat loss on evaporation efficiency should not be overlooked. Researchers have employed low thermal conductivity and insulating materials to reduce contact between the material and the bulk water, minimizing heat loss and effectively improving evaporation efficiency.[33–35] In recent years, significant progress has been made in the design and performance optimization of solar evaporators, especially in terms of local structural innovations.[36–39] However, several challenges must be addressed to further optimize solar evaporator technology, including overcoming deficiencies in existing structures to improve photothermal conversion efficiency. Additionally, to achieve efficient and stable operation of solar evaporators, it is crucial to optimize the light-absorbing materials, support substrates, thermal management systems, and water transport and salt barrier mechanisms in an integrated manner.[40–42] Currently, solving these problems remains a formidable challenge for researchers. Therefore, developing a simple and rapid method to prepare solar evaporators with stable structures, excellent evaporation efficiency, and high salt resistance (salinity >3.5 wt%) is of great importance. In this context, silicon-based glass emerges as a promising candidate for solar evaporation technology due to its distinctive physical and chemical attributes. The low thermal conductivity of silicon-based glass is instrumental in mitigating heat loss,[43] a critical factor in enhancing the thermal efficiency of solar evaporators. Its robust stability across a range of chemical environments, including acidic and alkaline conditions, confers an advantage in managing diverse water qualities, such as seawater and other impurity-laden sources. These intrinsic properties of silicon-based glass render it a pivotal material for the development of an efficient, stable, and durable solution for water evaporation in solar evaporator systems.

In this study, we have developed a porous glass evaporator (PGE) that demonstrates high efficiency in water evaporation. The fabrication of these evaporators involved a novel approach, blending glass powders with soluble salts and utilizing a dissolution-based fabrication method to create a structure with continuous pores. This approach eliminates the need for complex glass phase separation processes and avoids the generation of harmful waste. The resulting solar evaporator exhibits strong light absorption across a broad spectral range, from 0.3 to 2.5 µm, enhancing the photothermal conversion efficiency. The low thermal conductivity of the silica-based glass significantly reduces heat loss, allowing for the formation of localized heat surfaces and impressive thermal management capabilities. Microstructurally, the evaporator is engineered with a multitude of micrometer-scale pores that form interconnected porous channels. These channels not only facilitate efficient water transport through capillary action but also simultaneously prevent salt deposition. The internal network of interconnected micrometer-scale pores significantly enhances the water conveyance capabilities, making them more suitable for capillary pumping compared to nanoscale pores.[44] The innovative design and superior material properties of this interfacial solar evaporation system have resulted in exceptional performance in terms of water evaporation, salt tolerance, and deionization. Under one sun irradiation, the PGE exhibits exceptional solar evaporation capabilities, achieving a high rate of 2.21 kg m^{-2} h^{-1} in pure water with an evaporation efficiency of 98%, which highlights its superior energy conversion efficiency. In seawater, it operates at 2.08 kg m^{-2} h^{-1}, and in methylene blue solution, it reaches 2.47 kg m^{-2} h^{-1}, demonstrating impressive performance under standard solar intensity. Furthermore, the evaporator has demonstrated outstanding stability during evaporation, maintaining a consistent evaporation rate even after ten consecutive evaporation cycles. Even after following rigorous and prolonged exposure to a sequence of acidic and alkaline treatments, the PGE continues to manifest an exceptional evaporation rate exceeding 2.0 kg m^{-2} h^{-1}. The PGE's structural integrity remains intact even under such extreme conditions, which serves to enhance its exceptional performance retention. This robust behavior underscores the PGE's potential as a superior candidate for applications in harsh environments, where the material's reliability and robustness are crucial.

2. Results and Discussion

2.1. Fabrication and Characterization of PGE

The schematic illustration for fabricating a porous glass evaporator is presented in **Figure 1a**. The synthesis process involves thoroughly mixing the glass powder with a soluble powder. Upon heating to an appropriate temperature, the glass powder undergoes the thermoplastic deformation characteristic of amorphous materials, allowing it to flow and infiltrate the interstitial spaces among the NaCl particles. Subsequent cooling solidifies the mixture, after which the evaporator is submerged in water to facilitate the dissolution of the embedded NaCl, thereby creating a porous structure with internal connectivity. The PGE then demonstrates a visual effect of glossy black color, which can be placed on the leave (Figure 1b). As shown in Figure 1c, scanning electron microscopy reveals the microstructure of the porous glass evaporator, characterized by the presence of numerous micrometer-sized pores, confirming the effective porosity of the evaporator.

To confirm the presence of interconnected porous channels within the evaporator, permeability test was conducted. The evaporator was secured using clips, and a predetermined volume of water was dripped onto its upper surface. During a 15-min equilibration period, it was observed that the water droplets gradually infiltrated from the upper surface to the lower surface, as depicted in Figure 1d. This observation, as visualized in Video S1 (Supporting Information), suggests the presence of continuous channels within the material. As shown in Figure 1e, the examination of the micromorphology within the evaporator cross-section using scanning electron microscope (SEM) revealed a rich network of micrometer-sized pores in the cross-section. This finding suggests the presence of a continuous porous structure within the evaporator, which promotes efficient water transport and thus improves the efficiency of the desalination process.

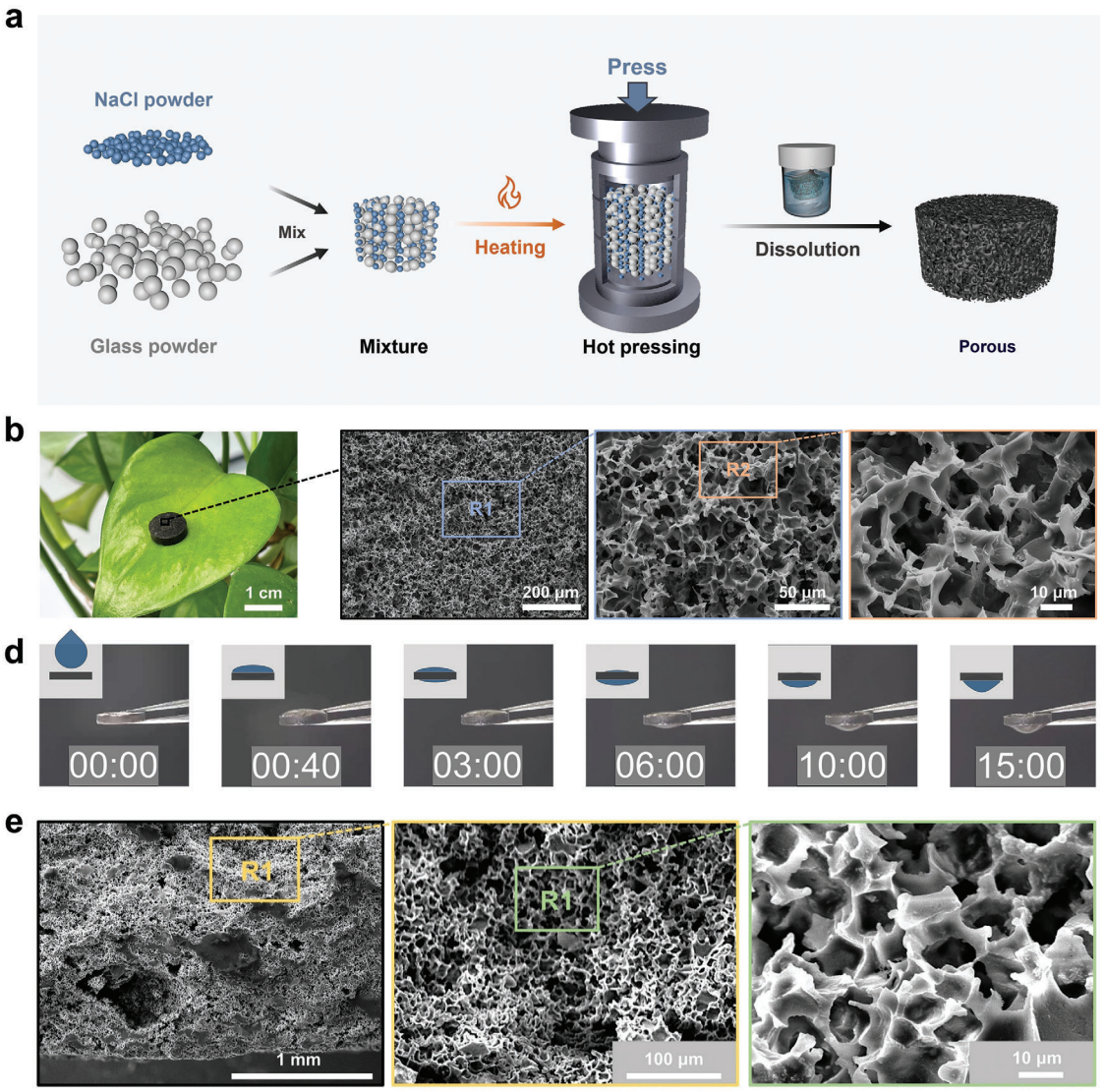

Figure 1. a) The schematic diagram for preparing PGE. b) PGE is placed on the leave. c) The SEM images of the micropore on the PGE. d) Water permeability verification of PGE. e) Cross-sectional SEM images of the micropore on the PGE.

2.2. The Photothermal Performance

The photothermal conversion performance of the evaporator plays a decisive role in solar-driven water evaporation. To assess the PGE's photothermal conversion capabilities, we documented the temperature changes on its surface under varying power inputs. Compare to the Glass-plate (GP) fabricated by hot pressing with glass powder (**Figure 2**a), Figure 2b a comparison of the temperature rise profiles of PGE and glass plate under the irradiation of 808 nm laser. At a laser power density of 0.5 W cm^{-2}, the PGE can achieve a temperature increase of around 80 °C. Moreover, it maintains stable and rapid temperature responses under rapid switching conditions, demonstrating excellent cycling stability. Figure 2c demonstrates a positive correlation between the 808 nm laser power density and the temperature rise observed in PGE, while maintaining a relatively stable and rapid response under rapid on/off conditions. As illustrated in Figure 2d, when the PGE is in a dry state under one sun illumination, the surface temperature of the GP reaches 57 °C, whereas the PGE surface temperature can reach 65 °C. The infrared image captures the temperature distribution of both the PGE and GP at a specific moment (Figure 2e), revealing that the porous structure plays a crucial role in enhancing the evaporator's temperature increase. This effect is attributed to the microstructured surface, which increases the surface roughness (Sa = 11.08 μm, Figure S1, Supporting Information), substantially reducing light reflection from the material's surface and allowing more light to enter the evaporator's interior, thus enhancing light absorption.

The solar absorption capacity of the evaporator is equally determinant for solar-driven water evaporation. A spectrophotometer equipped with an integrating sphere was used to measure the absorbance (A) and reflectance (R) of the PGE. Figure 2f; and Figure S2 (Supporting Information) illustrate the absorption and reflection properties of the PGE and GP. Across the spectrum from 200

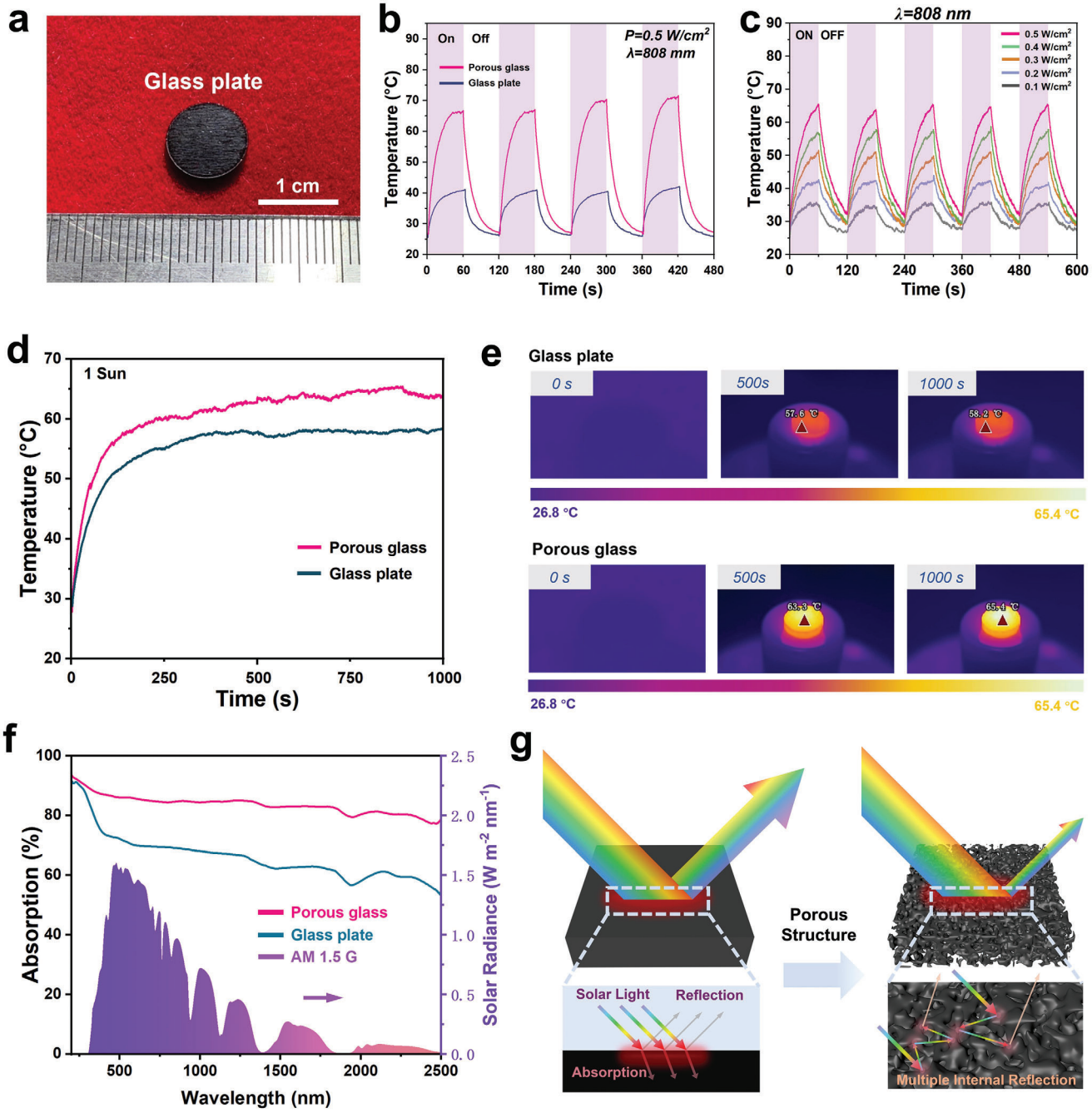

Figure 2. a) The photo of Glass-plate. b,c) Temperature rise curve of PGE and Glass-plate under different power irradiation density with an 808 nm laser. d) Temperature rise curve of PGE and Glass-plate under one sun solar irradiation. e) The temperature distribution infrared images of PGE and Glass-plate under one sun solar irradiation. f) Absorption spectra of the PGE. g) The absorption mechanism of the PGE.

to 2500 nm, the PGE exhibits a higher absorbance than the GP, primarily due to the enhanced light absorption resulting from the PGE's rich porous structure. The N_2 adsorption–desorption isotherms shown in Figure S3 (Supporting Information) indicate a specific surface area of 3.8 $m^2\ g^{-1}$ for the porous evaporator, with a hysteresis loop closing at a relative pressure of around $P/P_0 = 0.4$, suggesting the presence of mesopores and micropores with an irregular pore structure. This porous structure allows for multiple internal reflections of incident light within the sample, which is beneficial for improving photothermal conversion performance. Figure 2g depicting the illumination mechanism illustrates the enhanced absorption of the PGE. Within the PGE's porous structure, the multiple reflections of incident light result in a significant enhancement of absorption. The porous structure increases the scattering and reflection of light within the PGE. As light enters this structure, it bounces back and forth

between the pores, undergoing multiple reflections that lead to repeated absorption of the incident light, effectively preventing the escape of light and substantially increasing the PGE's light absorbance.[45,46] Due to its notable features, the PGE exhibits exceptional light absorption capabilities across a broad spectral range of 200–2500 nm, indicating its significant potential for applications in photothermal conversion technology.

The blackening of the evaporator during the thermoplastic forming process, resulting from high-temperature treatment, serves as a critical indicator of the photothermal effect.

To confirm and analyze the chemical composition of the blackened evaporator, we conducted energy-dispersive X-ray spectroscopy (EDS) analysis on both the untreated pristine glass sample and the PGE (Figures S4 and S5, Supporting Information). The comparative analysis of the EDS demonstrated that the elemental composition of the raw and heat-treated samples was unchanged, with no introduction of additional impurities. X-ray photoelectron spectroscopy (XPS) analysis (Figure S6, Supporting Information) was also performed, which helps to provide insight into the molecular changes occurring within the material. The analysis reveals a 77.82% increase in the peak area of C—C/C=C bonds at around 284 eV (Figure S7, Supporting Information) after high-temperature treatment. The substantial augmentation of C—C/C=C bond content signifies a profound enhancement of the conjugation effect within the material's molecular structure. This increased conjugation facilitates greater delocalization of π electrons, expanding the electron cloud and enabling the material to absorb light more effectively across a wider spectral range. The enhanced light absorption translates into more efficient conversion of absorbed energy into heat, thereby directly promoting a stronger photothermal response.

2.3. Solar-Driven Water Evaporation

Drawing on the photothermal capabilities and the intricate porous architecture of PGE, a comprehensive set of experimental assessments was carried out to measure its efficacy in solar-driven evaporation. The evaporator was embedded within the sunken cavity of a highly water-absorbent sponge to assess its temperature rise and water evaporation performance. Under solar irradiation equivalent to one sun, the surface temperature of the evaporator swiftly rose to 40 °C within the first 5 min, ultimately attaining a state of equilibrium after 15 min (**Figure 3a**). The effective localization of heat generated by the solar thermal effect on the evaporator's surface resulted in a stable temperature of ≈45 °C throughout the evaporation process. In contrast, under the same lighting conditions, the temperature of pure water increased incrementally during evaporation, reaching only about 30 °C after an hour. This clearly demonstrates that the surface temperature of the evaporator significantly exceeded that of the pure water during the evaporation process. To ascertain the solar-driven water evaporation performance of PGE, we independently constructed an evaporation experiment setup to record the mass changes occurring during the evaporation process (Figure S8, Supporting Information). As shown in Figure 3b, the PGE achieves a stable evaporation rate of 2.21 kg m^{-2} h^{-1} under one sun illumination, which is 4.51 times that of pure water (0.49 kg m^{-2} h^{-1}). The underlying cause for this discrepancy lies in the fact that, under solar irradiation, the surface temperature of the PGE surpasses that of pure water, thereby accelerating the rate of water vapor escape.

2.4. Evaporation Stability

To assess the stability of the PGE's evaporation performance under simulated solar irradiation, a series of experiments were designed with the evaporator subjected to irradiation intensities of 1 sun, 3 sun, and 5 sun. The experimental results (Figure 3c) revealed a significant increase in evaporation rate as the irradiation power density increased to 5 sun. Additionally, the shape of the evaporation curves remained consistent across all irradiation conditions, with no abrupt fluctuations or performance degradation observed, indicating that the tested PGE exhibits good evaporation stability within the range of irradiation tested.

To assess the evaporation performance and the evaporation stability of the PGE, we designed evaporation tests in three distinct media: pure water, 3.5 wt% sodium chloride solution, and methylene blue solution (Figure 3d–f). Furthermore, we evaluated its reusability under solar irradiation (Figure 3g–i). The PGE maintained consistent evaporation rates even after 10 cycles (Figures S9,S10, and S11, Supporting Information), demonstrating its durability and robust performance across various conditions. The environmental temperature and humidity were set at 26 °C and 50%, respectively, ensuring reliable experimental results.

2.5. Desalination Performance

In the simulated seawater desalination experiment, we selected five major metal ions (Na^+, K^+, Mg^{2+}, Ca^{2+}, and B^{3+}) to characterize the desalination capabilities of the PGE. The evaporated water was collected through a collection device (Figure S12, Supporting Information) that we assembled. To comprehensively evaluate the desalination efficacy, natural seawater from the Yellow Sea in China was employed for assessment, which was subsequently analyzed using inductively coupled plasma mass spectrometry (ICP-MS). As depicted in Figure 3j, postdesalination, the concentrations of metal ions in the water samples were significantly reduced compared to the untreated water. The initial concentrations of Na^+, Mg^{2+}, K^+, and Ca^{2+} were 10 000, 1300, 430, and 380, respectively, all of which exceeded the World Health Organization's (WHO) drinking water standards, which are 50, 10, 100, and 100, respectively. Following evaporation, the concentrations of Na^+, Mg^{2+}, K^+, and Ca^{2+} in the water were found to be 9.85, 1.85, 0.86, and 0.25, respectively, all of which are significantly lower than the WHO's drinking water standard concentrations, indicating a remarkable desalination effect. The concentration of B^{3+} was measured to have decreased from 6.5 mg L^{-1} before evaporation to 0.38 mg L^{-1} after evaporation. This demonstrates that the PGE effectively removes these metal ions from the water, significantly reducing their concentrations to levels that are safe for human consumption as defined by the WHO. The PGE's ability to efficiently remove these ions suggests its potential for large-scale seawater desalination, addressing the pressing issue of water scarcity and providing a sustainable source of freshwater.

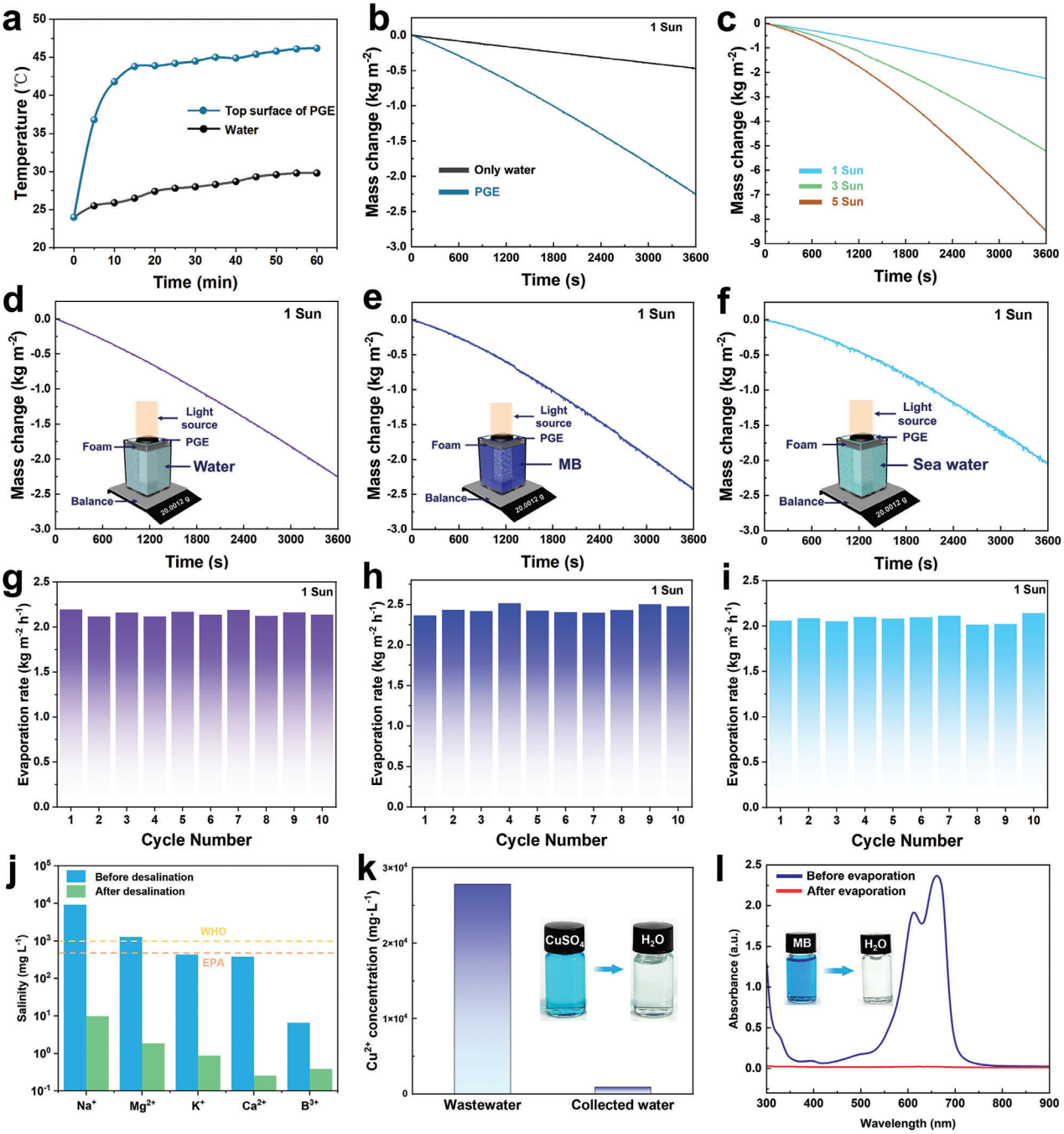

Figure 3. a) The surface temperature change curves. b) Mass change of water over time of PGE and pure water under one sun solar irradiation. c) Mass change of water over time for the PGE under different sun irradiation. d–f) Mass change of water over time of PGE in pure water, MB and seawater under one solar irradiation. g–i) Stability of PGE in pure water, MB and seawater under one solar irradiation for ten cycles. j) The concentrations of Na^+, Mg^{2+}, K^+, and Ca^{2+} in actual seawater samples (Huanghai Sea) before and after desalination, the dashed line represents the WHO and EPA standards. k) The concentrations of Cu2+ in wastewater and collected water. l) UV–vis–NIR absorption spectra of MB and evaporated water.

Although present in trace amounts, heavy metals are highly toxic, ubiquitous, and can have detrimental effects on human health and the environment. For instance, copper ions can lead to liver damage, insomnia, and inhibit soil enzyme activity. To simulate heavy metals in electrolytes, $CuSO_4{\cdot}5H_2O$ was employed. As illustrated in the inset of Figure 3k, following solar-driven evaporation, the color of the copper electrolyte shifted from blue to transparent, with the concentration of copper ions (Cu^{2+}) decreasing from 20 000 to 900 mg L^{-1}. The removal efficiency of Cu^{2+} from wastewater reached over 95%, which is a remarkable outcome.

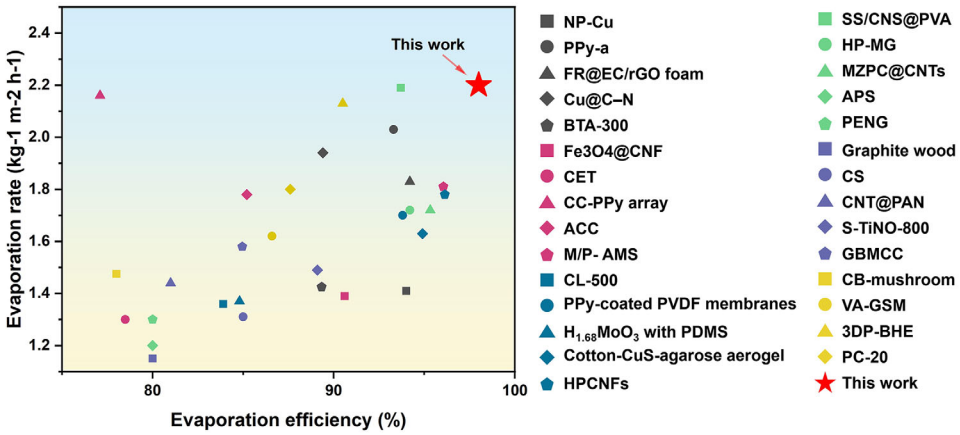

Figure 4. The comparison of the evaporation efficiency and evaporation rate of the previous materials.

2.6. Wastewater Treatment Performance

In addition to water scarcity, water pollution is a pivotal factor contributing to the global strain on resources. The dye content within industrial wastewater is a significant contributor to environmental pollution. In the present study, a methylene blue solution was employed as a surrogate for wastewater to assess the treatment efficacy of polluted water through the evaporation process. By comparing the color changes of the solution before and after evaporation with the condensate, it was observed that the condensed water emerged as clear and transparent, indicating that the PGE is effective in treating dye-contaminated wastewater. To further corroborate the nature of the condensate, spectral scans of the original solution and the condensate were conducted using an ultraviolet–visible–infrared spectrophotometer. Ultraviolet–visible spectroscopic analysis revealed the absence of characteristic absorption peaks of the wastewater solution in the condensate, with an absorption profile akin to pure water (Figure 3l). Consequently, it can be inferred that the PGE efficiently segregates water molecules from organic dye-contaminated wastewater via evaporation, yielding water of high purity. This separation is achieved through the physical process of evaporation, where water molecules are heated and vaporized, leaving the nonvolatile solutes in the original liquid, significantly reducing their concentration in the condensed and collected fresh water.

2.7. Evaporation Efficiency

Benefiting from its excellent photothermal properties and superior water transport capabilities, the PGE exhibited a high evaporation rate under one sun illumination. Due to its high solar absorption rate, the wet PGE maintained a stable surface temperature of 45.1 °C under 1 kW m^{-2} sunlight (Figure 3a). The solar energy conversion efficiency (η) of the evaporation system can be calculate by the following equation:[34]

$$\eta = \dot{m} h_{LV} / C_{opt} P_o \quad (1)$$

$$\dot{m} = m_{Lig/ht} / m_{Dark} \quad (2)$$

$$h_{LV} = L_V + C\Delta T \quad (3)$$

The $\dot{m}$ in the equation represents the actual rate of evaporation of water (kg m^{-2} h^{-1}) which has subtracted the evaporation rate under dark condition (Figure S13, Supporting Information); h_{LV} denotes the total enthalpy of liquid vapour conversion with sensible and latent heat enthalpies; C_{opt} is the light concentration factor of the sunlight simulator and P_0 is the solar light intensity of 1 kW m^{-2}. The evaporation efficiency of PGE is calculated by the above equations to be 98.04% (The detailed calculations are shown in Note S1, Supporting Information).

To substantiate the superlative nature of our fabricated solar-driven water evaporation porous material, we have compiled a summary of the evaporation performance of previously investigated materials for solar water evaporation (**Figure 4**; and Table S1, Supporting Information). In a comparative analysis with metallic photothermal materials, carbon-based photothermal materials, and gel photothermal materials, our material emerges as a standout, exhibiting a remarkable evaporation rate and a satisfying evaporation efficiency among the diverse array of materials surveyed. We have also compared our evaporation rate with those reported works conducted under humidity conditions that are similar to or lower than those in the present study. Upon comparison (Table S2, Supporting Information), our evaporation rates exhibit a distinct advantage. Under humidity conditions that are comparable, or even more favorable or lower, our evaporation rate surpasses those previously reported.

2.8. Water Transport Capacity

In the design of solar steam generators, a crucial parameter for ensuring efficient vapor production is the device's water supply capability, with hydrophilicity being a key attribute for achieving this functionality. This study evaluated the wettability of the glass slide and the porous glass evaporator surface using contact angle tests. The experimental results shown in **Figure 5a** reveal that water droplets were swiftly absorbed within 0.2 s upon contact with the PGE surface, indicative of the material's exceptional superhydrophilicity. In contrast, a stable water droplet shape was formed on the glass slide surface, with a contact angle measurement of ≈51°. The capillary forces induced by the interconnected

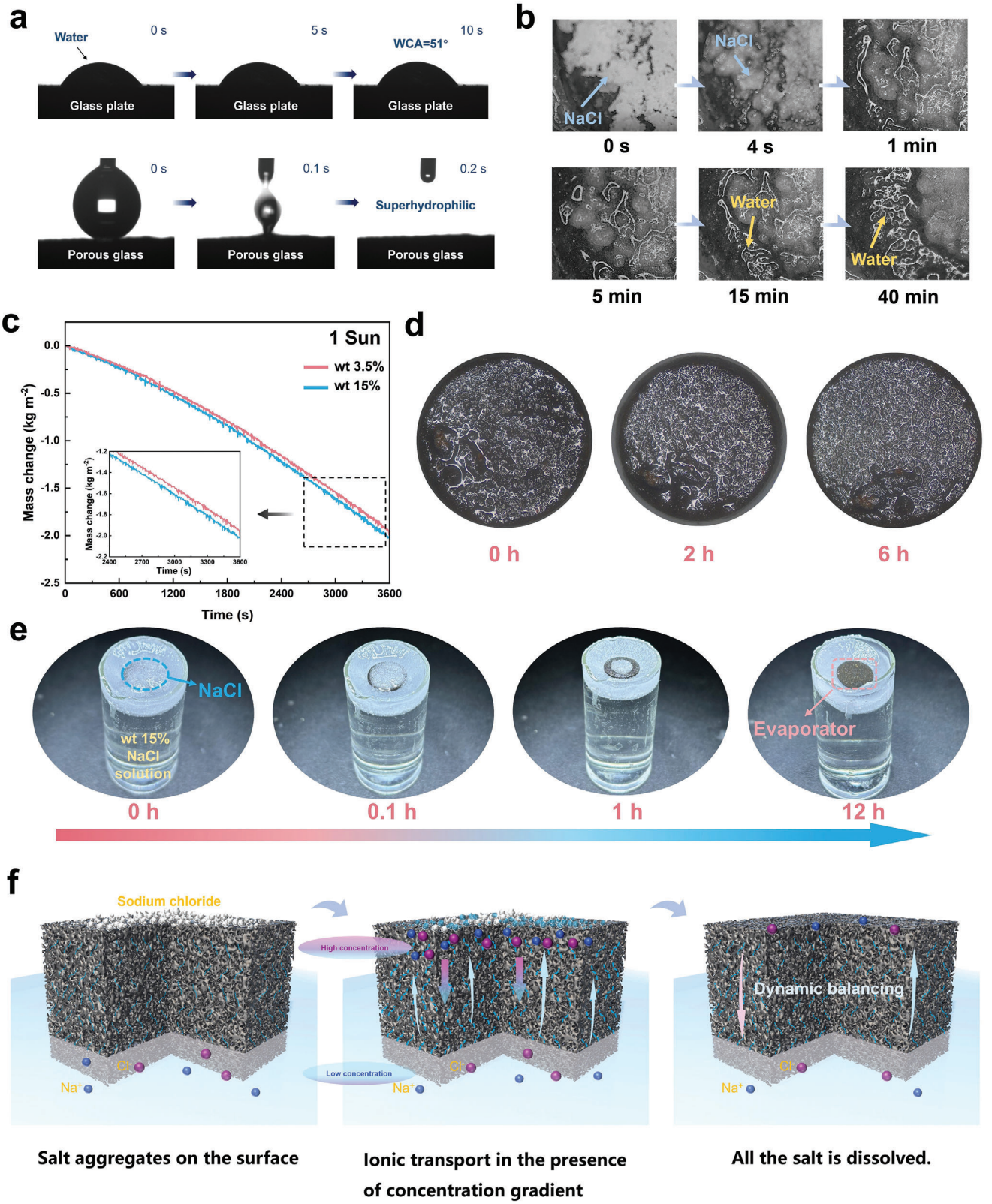

Figure 5. a) The evolution of water angle on Glass plate and PGE. b) Optical photograph of PGE surface simulating dissolution changes of accumulated salt. c) Mass change of simulated seawater of wt 3.5% and wt 15% over time of PGE. d) Snapshot of the evaporation process of PGE (top) in wt 15% simulated seawater. e) Optical photograph of PGE surface simulating dissolution changes of accumulated salt in wt 15% simulated seawater. f) Schematic diagram of the transport processes of salt and water.

pore network within the evaporator, coupled with the intrinsic hydrophilicity of the silicon-based substrate stemming from its copious silicon-oxygen bonds, enable the swift absorption of water droplets, culminating in a superhydrophilic surface. This superhydrophilic surface ensures a timely water supply for the evaporation process.[47] Furthermore, the porous internal structure of the evaporator facilitates the flow of liquid along the pore walls through capillary suction, effectively transporting water from the bottom to the top and preventing salt accumulation at the top surface.[48,49] As depicted in Figure S14 and Video S2 (Supporting Information), a thin sheet of paper was positioned atop the porous evaporator, with a shallow layer of methylene blue solution placed beneath the evaporator in a separate container. Upon carefully submerging the evaporator into the solution, the solution quickly penetrated through the complex interconnected pore network of the evaporator structure. This rapid capillary action brought the solution to the surface of the evaporator, where it spread from the middle of the paper to the edges. In summary, the solar evaporator can rapidly transport water to the evaporation surface. The interconnected network of micrometer-sized pores within the porous structure not only provides a larger effective surface area for capillary action but also facilitates water diffusion.[44] Therefore, the evaporator's excellent hydrophilicity combined with its internal porous structure provides an effective water transport channel and ensures efficient water delivery for the evaporation process.

2.9. The Salt Resistance

Furthermore, the PGE demonstrates a commendable resistance to salt accumulation under prolonged solar illumination. As depicted in Figure 1e, the PGE is characterized by a porous network, with its interior embellished by micrometer-scale pores that are interconnected to form porous channels. These channels furnish a structural framework and conduits for the diffusion of water molecules. Consequently, liquid swiftly ascends along the channels toward the surface, where water molecules are transformed into water vapor through evaporation. Subsequently, water molecules at the bottom continue to replenish the evaporation surface, ensuring a sustained water supply. This mechanism significantly mitigates salt accumulation.[50] As evidenced in Figure 5b, when solid salt is directly deposited atop the evaporator's surface, the majority of the salt dissolves within 40 min, underscoring the PGE's robust resistance to salt accumulation.

Moreover, the evaporator did not accumulate salt and experienced no significant decrease in evaporation rate across various concentrations of saltwater. As illustrated in Figure 5c, when 15 wt% pure NaCl solution served as the feedstock, the evaporation rate was nearly equivalent to that when 3.5 wt% NaCl solution was used, reaching 2.0 kg m^{-2} h^{-1}. This finding further indicates that the evaporator's rate of evaporation remains relatively unchanged in high-concentration saltwater. The slight reduction in the rate is primarily due to the reduced concentration gradient between the saltwater at the bottom and the saltwater at the top of the evaporator, which slows down the rate of water transport. As illustrated in Figure 5d, even after continuous operation for 6 h, no salt crystals were observed on the surface of the evaporator, further confirming its robust resistance to salt accumulation in high concentration saltwater. Figure 5e illustrates a test to validate the evaporator's resistance to salt accumulation in high concentration saltwater. The evaporator was submerged in a 15 wt% NaCl solution, and a solid salt was placed directly on its surface. Under the influence of the concentration gradient, the salt on the surface dissolved gradually. Within 12 h, all the salt particles on the surface were completely dissolved, underscoring the evaporator's capability to resist salt accumulation even under high concentration conditions. Figure 5f elucidates the diffusion process of salt ions within the evaporator and further analyzes the mechanism of its salt resistance. The evaporation of water at the upper surface of the evaporator leads to an increase in the concentration and density of ions at the surface, creating ion concentration and density gradients between the upper and lower parts of the evaporator. Driven by the gradient effect, salt ions diffuse from areas of high concentration to areas of low concentration.[38,51] Leveraging the continuous channels formed by the porous structure within the evaporator, salt ions are allowed to diffuse through the porous channels into the bulk water. This creates a dynamic equilibrium between ion convection within the structure and the diffusion of salt ions driven by the gradient effect, making it difficult for salt crystals to nucleate and accumulate on the evaporator's surface. This mechanism prevents the accumulation of salt crystals that could potentially block the channels.

2.10. Thermal Energy Management

Thermal management is a critical factor in evaluating solar-driven interfacial evaporators. Low thermal conductivity materials can effectively reduce heat transfer and loss, concentrating heat at the gas–liquid interface, which is beneficial for the formation of localized heating zones on the evaporator's surface. As depicted in **Figure 6**a, under dry conditions, the alternating illumination process was recorded using an infrared imager under vertical irradiation with a 808 nm laser at a power density of 1 W cm^{-2}. As shown in the heat distribution, the surface temperature of the evaporator rapidly increased to 130 °C within 60 s, quickly reaching thermal equilibrium, indicating a very fast response time for photothermal conversion. Meanwhile, the region near the bottom of the evaporator's side only reached a temperature of 60 °C within the same timeframe. Under wet conditions, when irradiated vertically with a 808 nm laser at a power density of 1 W cm^{-2}, the surface temperature of the evaporator also demonstrated rapid heating capabilities, reaching 81 °C within 60 s. Similarly, the region near the bottom of the side of the evaporator only reached 45 °C during the same period. These observations indicate that, regardless of whether the evaporator is dry or wet, a significant temperature difference is established between the top and bottom of the device, effectively confining the heat to the top of the evaporator, which is conducive to the formation of a localized heating zone and significantly reduces heat loss. This enhances the evaporator's thermal management capabilities. Furthermore, the temperature gradient created between the surface and bottom of the evaporator by light radiation triggers the Marangoni effect.[38] This temperature-induced convection accelerates the internal water flow within the evaporator, further enhancing the velocity of salt ion convection. This, in turn, bolsters the evaporator's resistance to salt accumulation, thereby

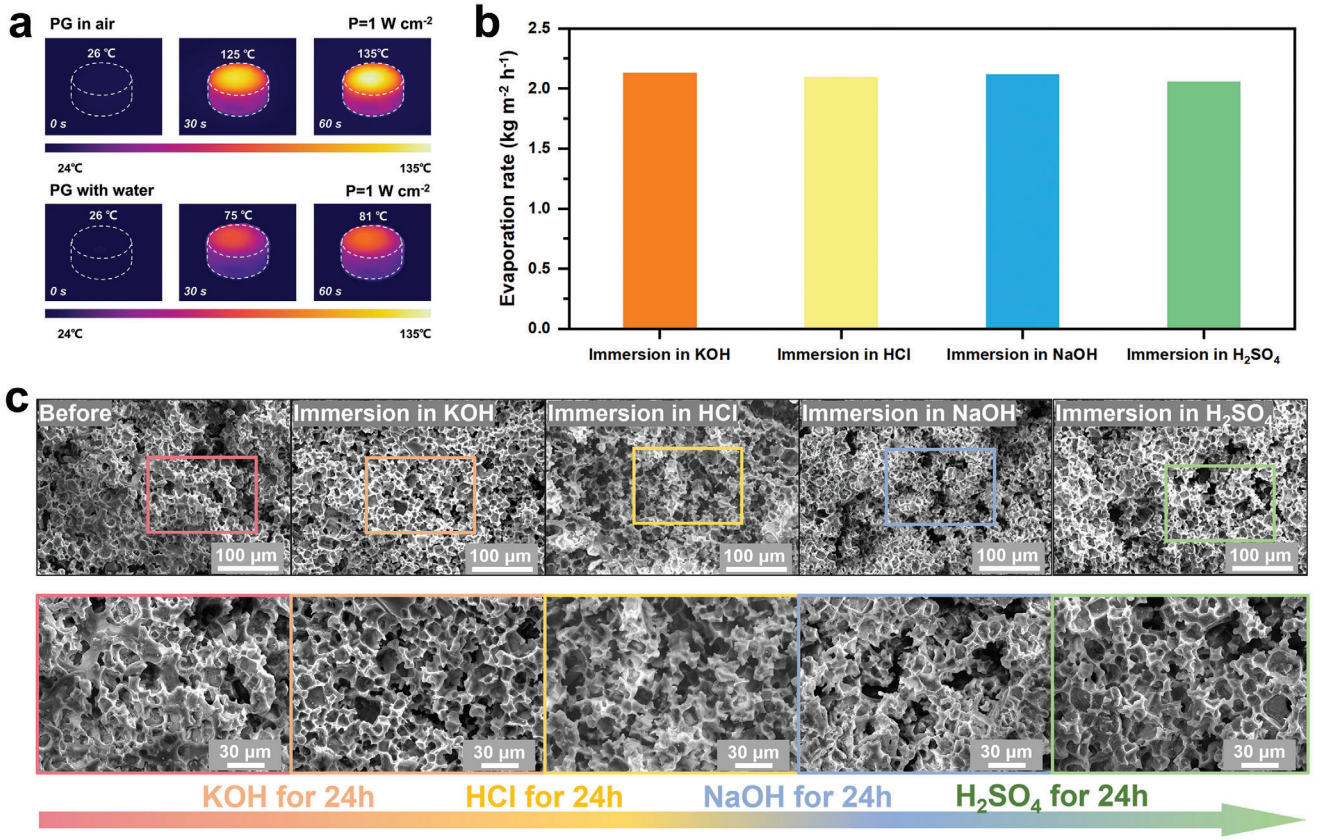

Figure 6. a) The temperature distribution infrared images of PGE in air and water under 1 W cm^{-2} irradiation with an 808 nm laser. b) Evaporation rates of PGE after alternating immersion in extreme environment. c) The SEM images of PGE after alternating immersion in extreme environment.

improving its performance in maintaining high-efficiency evaporation in the presence of salts.

2.11. Evaporation Performance in Extreme Environments

In investigating the adaptability of the PGE to harsh environments, this study simulated the conditions that might be encountered in practical applications by alternately immersing PGE in acidic and alkaline media. Specifically, PGE samples were immersed in KOH (1 M), HCl (1 M), NaOH (1 M), and H_2SO_4 (1 M) solutions for 24 h each, and then the surface structure and evaporation rate were assessed after the treatments. As depicted in Figure 6b, even after exposure to acidic and alkaline treatments, the evaporation performance maintains a high rate exceeding 2.0 kg m^{-2} h^{-1}, and the morphology of the porous structure of the PGE (Figure 6c) remains intact, demonstrating excellent stability. This finding highlights the potential of the PGE in real-world applications, particularly in environments that demand high material performance, where the PGE has demonstrated exceptional environmental tolerance and stability.

3. Conclusion

In this work, the PGE with exceptional photothermal conversion efficiency and resilience against salt accumulation for efficient and sustainable water purification and desalination was fabricated. The PGE's unique structure, characterized by continuous porosity and an interconnected pore network, enables efficient water transport, ensuring a continuous supply to the evaporation surface. This not only enhances the evaporation rate but also mitigates the risk of salt accumulation, thereby maintaining the device's performance over extended periods. Moreover, the PGE's robustness in various environmental conditions, as evidenced by its stability in both acidic and alkaline media, underscores its potential for practical applications in diverse settings. Its ability to maintain its structure and performance even after exposure to extreme conditions highlights its durability and reliability. In conclusion, the PGE represents a significant advancement in the field of solar driven water evaporation and purification. Its innovative design, coupled with its exceptional performance, makes it a promising candidate for large scale water treatment and desalination, offering a sustainable and environmentally friendly solution to the pressing issue of water scarcity. Further research and development are warranted to fully harness the potential of the PGE and to explore its applications in broader contexts.

4. Experimental Section

Materials: The D-K59 glass was selected for this study due to its lower glass transition temperature (T_g) compared to the melting point of sodium chloride, allowing it to soften prior to the softening of sodium

chloride. This characteristic endows the glass with superior thermoplastic forming capabilities. NaCl was purchased from Maclean Biochemical Technology Co. Ltd in Shanghai. NaCl powder requires recrystallization and grinding to prepare particles with a particle size of ≈30 µm.

Preparation of PGE: The prepared glass powders with a diameter of 100 µm and NaCl powders with a diameter of 30 µm were compounded in a mass ratio of 3:1 within a powder mixing apparatus to achieve a uniform mixture. The well-dispersed powder blend was then transferred into a mold and subjected to a vacuum environment with a pressure of 3×10^{-3} Pa within a heating chamber. Upon reaching the optimal thermoplastic temperature of 923 K, a compressive force of 64 MPa was applied to the mold, and the temperature and pressure were conserved for a period of 15 min to facilitate the shaping process under thermoplastic conditions. Following the shaping protocol, the temperature was lowered to 553 K, at which stage the sample was extracted from the heating chamber. Postcooling, the sample was immersed in an 80 °C water bath for 30 min to facilitate the removal of the NaCl particles from the composite matrix.

Multiscale Characterization: The morphology and structure of the evaporator were examined using a SEM (Fei Quanta FEG 450). The absorbance (A) and reflectance (R) of the evaporator were measured with a UV–vis–NIR spectrophotometer equipped with an integrating sphere (Shimadzu UV-3600). Transmission electron microscopy (TEM, JEOL JEM-2011F, 200 kV) equipped with energy-dispersive X-ray spectroscopy (EDS) was used to investigate elemental mapping. The surface composition and valence states of the different elements were analyzed by X-ray photoelectron spectroscopy (XPS, Thermo Scientific K-Alpha). The temperatures of the PGE and GP were recorded using an infrared thermal imager (Fotric 280d). The concentrations of Na^+, K^+, Ca^{2+}, Mg^{2+}, and B^{3+} in the samples were determined by inductively coupled plasma optical emission spectrometry (ICP–OES). Absorption spectra of the dye MB and condensate were measured from 200 to 900 nm using a UV–vis–NIR spectrophotometer (Shimadzu UV-1280). The contact angle (CA) on the surface of the evaporator was measured using a drop shape analyzer (DSA100S, Krüss, Germany) with a 3 µL water droplet volume.

Water Evaporation Characterization: To simulate solar radiation, a Xe light source equipped with an AM 1.5 filter (CEL-HXF 300, Beijing Education Au-light Co., Ltd.), which was positioned above the sample was employed. The light intensity was measured using a high-performance photodiode power meter (CEL-NP2000, Beijing Education Au-light Co., Ltd.). To monitor temperature changes during evaporation, an infrared thermal imager was utilized. Additionally, a high-precision electronic balance (Sartorius Quintix35-1CN, with a measurement accuracy of 0.01 mg) connected to a computer enabled precise measurement of the sample's mass loss during evaporation. When the PGE was embedded in the sponge's concave cavity, water within the sponge permeated from the bottom to the surface of the PGE. The xenon light source was then activated and adjusted to an intensity equivalent to one sun. During this process, the pure water evaporated into steam, leading to a decrease in the mass of water in the glass bottle. Considering that the water absorbed in the sponge would also heat up and evaporate under the simulated sunlight, to ensure the accuracy of the evaporation measurement, the glass bottle and the portions of the sponge other than the sample were wrapped in aluminum foil, ensuring that only the sample surface was exposed to the light. The experimental conditions were controlled at an ambient temperature of 26 °C and humidity of 50%, ensuring consistent results.

The Photothermal Characterization: To evaluate the photothermal conversion performance of the PGE, it was placed on a quartz slide and exposed to 808 nm laser radiation at varying power densities. Infrared imaging technology was employed to monitor the temperature changes on the surface of the sample in real time. The experimental setup involved subjecting the sample on the quartz substrate to laser irradiation cycles of 60 s each, with a total duration of 480 s for each set power density. Throughout the irradiation period, an infrared imaging camera continuously recorded the thermal response of the sample surface at a sampling rate of 3 Hz.

Supporting Information

Supporting Information is available from the Wiley Online Library or from the author.

Acknowledgements

The work was financially supported by the Key Basic and Applied Research Program of Guangdong Province, China (Grant No. 2019B030302010), the NSF of China (Grant Nos. 52122105, 52130108, 523B2006, and 52271150), the Science and Technology Innovation Commission Shenzhen (Grants Nos. RCJC20221008092730037 and 20220804091920001) and the Research Team Cultivation Program of Shenzhen University (Grant No. 2023QNT001). The authors thanked Instrumental Analysis Center of Shenzhen University for the assistance with the Electron Microscope.

Conflict of Interest

The authors declare no conflict of interest.

Author Contributions

J.L. and W.R. contributed equally to this work. J.L. and J.M. conceived the idea. J.M., W.R., H.Z., J.F., and F.S. supervised the work. J.L., H.Z., W.R., and Y.Z. designed experimental steps. J.L., H.Z., W.R., and J.W. completed the data analysis. L.Z. and J.H. performed SEM. J.L. and J.M. wrote the manuscript. J.M. reviewed and revised the manuscript. All authors contributed to the discussion and analysis of the results.

Data Availability Statement

Research data are not shared.

Keywords

evaporator, extreme environments, photothermal conversion, porous glass

Received: August 21, 2024
Revised: October 26, 2024
Published online: November 13, 2024

[1] C. Dang, Y. Cao, H. Nie, W. Lang, J. Zhang, G. Xu, M. Zhu, *Nat. Water* **2024**, *2*, 115.
[2] C. He, Z. Liu, J. Wu, X. Pan, Z. Fang, J. Li, B. A. Bryan, *Nat. Commun.* **2021**, *12*, 4667.
[3] A. E. Burakov, E. V. Galunin, I. V. Burakova, A. E. Kucherova, S. Agarwal, A. G. Tkachev, V. K. Gupta, *Ecotoxicol. Environ. Saf.* **2018**, *148*, 702.
[4] W. S. Chai, J. Y. Cheun, P. S. Kumar, M. Mubashir, Z. Majeed, F. Banat, S.-H. Ho, P. L. Show, *J. Clean. Prod.* **2021**, *296*, 126589.
[5] P. Tao, G. Ni, C. Song, W. Shang, J. Wu, J. Zhu, G. Chen, T. Deng, *Nat. Energy* **2018**, *3*, 1031.
[6] G. Alva, L. Liu, X. Huang, G. Fang, *Renewable Sustainable Energy Rev.* **2017**, *68*, 693.

[7] N. Kannan, D. Vakeesan, *Renewable Sustainable Energy Rev.* **2016**, *62*, 1092.
[8] H. Zhang, X. Shen, E. Kim, M. Wang, J. H. Lee, H. Chen, G. Zhang, J. K. Kim, *Adv. Funct. Mater.* **2022**, *32*, 2111794.
[9] M. Gao, L. Zhu, C. K. Peh, G. W. Ho, *Energy Environ. Sci.* **2019**, *12*, 841.
[10] J. Zhou, Y. Gu, P. Liu, P. Wang, L. Miao, J. Liu, A. Wei, X. Mu, J. Li, J. Zhu, *Adv. Funct. Mater.* **2019**, *29*, 1903255.
[11] M. Wang, Y. Wei, R. Li, X. Wang, C. Wang, N. Ren, S.-H. Ho, *Research* **2023**, *6*, 0290.
[12] X. Wu, Y. Lu, X. Ren, P. Wu, D. Chu, X. Yang, H. Xu, *Adv. Mater.* **2024**, *36*, 2313090.
[13] Y. Lu, D. Fan, Y. Wang, H. Xu, C. Lu, X. Yang, *ACS. Nano* **2021**, *15*, 10366.
[14] T. Li, H. Liu, X. Zhao, G. Chen, J. Dai, G. Pastel, C. Jia, C. Chen, E. Hitz, D. Siddhartha, R. Yang, L. Hu, *Adv. Funct. Mater.* **2018**, *28*, 1707134.
[15] G. Chen, Z. Jiang, A. Li, X. Chen, Z. Ma, H. Song, *J. Mater. Chem. A* **2021**, *9*, 16805.
[16] J. Yang, X. Suo, X. Chen, S. Cai, X. Ji, H. Qiao, *Adv. Sustainable Syst.* **2021**, *6*, 2100350.
[17] Z. Guo, J. Wang, Y. Wang, J. Wang, J. Li, T. Mei, J. Qian, X. Wang, *Chem. Eng. J.* **2022**, *427*, 131008.
[18] X. Yang, Y. Yang, L. Fu, M. Zou, Z. Li, A. Cao, Q. Yuan, *Adv. Funct. Mater.* **2017**, *28*, 1704505.
[19] B. Yu, Y. Wang, Y. Zhang, Z. Zhang, *Nano-Micro. Lett.* **2023**, *15*, 94.
[20] J. Fu, Z. Li, X. Li, F. Sun, L. Li, H. Li, J. Zhao, J. Ma, *Nano Energy* **2023**, *106*, 108019.
[21] B. Yu, Y. Wang, Y. Zhang, Z. Zhang, *Nano Res.* **2022**, *16*, 5610.
[22] X. Wu, C. Li, Z. Zhang, Y. Cao, J. Wang, X. Tian, Z. Liu, Y. Shen, M. Zhang, W. Huang, *Carbon Energy* **2024**, *6*, 466.
[23] F. Liu, B. Zhao, W. Wu, H. Yang, Y. Ning, Y. Lai, R. Bradley, *Adv. Funct. Mater.* **2018**, *28*, 1803266.
[24] L. Zhu, M. Gao, C. K. N. Peh, X. Wang, G. W. Ho, *Adv. Energy Mater.* **2018**, *8*, 1702149.
[25] S. Zhang, M. Li, C. Jiang, D. Zhu, Z. Zhang, *Adv. Sci.* **2024**, *11*, 2308665.
[26] Z. Yu, R. Gu, Y. Tian, P. Xie, B. Jin, S. Cheng, *Adv. Funct. Mater.* **2022**, *32*, 2108586.
[27] C. Gao, Y. Li, L. Lan, Q. Wang, B. Zhou, Y. Chen, J. Li, J. Guo, J. Mao, *Adv. Sci.* **2023**, *11*, 2306833.
[28] X. Chen, N. Yang, Y. Wang, H. He, J. Wang, J. Wan, H. Jiang, B. Xu, L. Wang, R. Yu, L. Tong, L. Gu, Q. Xiong, C. Chen, S. Zhang, D. Wang, *Adv. Mater.* **2021**, *34*, 2107400.
[29] W. Ruan, H. Zhang, J. Fu, Z. Li, J. Huang, Z. Liu, S. Zeng, Z. Chen, X. Li, Z. Yu, X. Liang, J. Ma, *Adv. Funct. Mater.* **2023**, *34*, 2312314.
[30] Y. Sun, D. Qu, W. Liu, L. An, X. Wang, Z. Sun, *Sci. China Mater.* **2023**, *66*, 4834.
[31] R. Wang, J. Deng, P. Wu, Q. Ma, X. Dong, W. Yu, G. Liu, J. Wang, L. Liu, *Energy Environ. Mater.* **2023**, *7*, e12667.
[32] Y. Lu, X. Wang, D. Fan, H. Yang, H. Xu, H. Min, X. Yang, *Sustainable Mater. Technol.* **2020**, *25*, e00180.
[33] T. Meng, B. Jiang, Z. Li, X. Xu, D. Li, J. Henzie, A. K. Nanjundan, Y. Yamauchi, Y. Bando, *Nano Energy* **2021**, *87*, 106146.
[34] Q. Feng, S. Tan, J. Lu, J. Li, J. Wang, C. Chen, W. Wu, Z. Xu, *ACS. Sustain. Chem. Eng.* **2024**, *12*, 3331.
[35] L. Cui, P. Wang, H. Che, J. Chen, B. Liu, Y. Ao, *Chem. Eng. J.* **2023**, *477*, 147158.
[36] J. Wang, X. Cao, X. Cui, H. Wang, H. Zhang, K. Wang, X. Li, Z. Li, Y. Zhou, *Adv. Mater.* **2024**, *36*, 2311151.
[37] X. P. Li, X. Li, H. Li, Y. Zhao, J. Wu, S. Yan, Z. Z. Yu, *Adv. Funct. Mater.* **2021**, *32*, 2110636.
[38] J. Wu, Z. Cui, Y. Yu, B. Yue, J. Hu, J. Qu, J. Li, D. Tian, Y. Cai, *Adv. Sci.* **2023**, *10*, 2305523.
[39] Y. Wang, C. Wang, X. Song, M. Huang, S. K. Megarajan, S. F. Shaukat, H. Jiang, *J. Mater. Chem. A* **2018**, *6*, 9874.
[40] F. Wang, S. Zhao, X. Zhang, Z. Su, *Desalination* **2022**, *543*, 116085.
[41] Z. Lei, B. Hu, P. Zhu, X. Wang, B. Xu, *Nano Energy* **2024**, *122*, 109307.
[42] S. Chaule, J. Kang, J.-H. Jang, *Mater. Today Energy* **2024**, *43*, 101588.
[43] H. Zhang, Y. Wang, Y. Liu, M. Zhao, C. Liu, Y. Wang, M. K. Albolkany, N. Wu, M. Wang, L. Yang, B. Liu, *ChemSusChem* **2020**, *13*, 2945.
[44] Y. Ito, Y. Tanabe, J. Han, T. Fujita, K. Tanigaki, M. Chen, *Adv. Mater.* **2015**, *27*, 4302.
[45] K. Li, T. H. Chang, Z. Li, H. Yang, F. Fu, T. Li, J. S. Ho, P. Y. Chen, *Adv. Energy Mater.* **2019**, *9*, 1901687.
[46] Z. Lei, X. Sun, S. Zhu, K. Dong, X. Liu, L. Wang, X. Zhang, L. Qu, X. Zhang, *Nano-Micro Lett.* **2021**, *14*, 10.
[47] P. Zhang, J. Li, L. Lv, Y. Zhao, L. Qu, *ACS Nano* **2017**, *11*, 5087.
[48] H. Ghasemi, G. Ni, A. M. Marconnet, J. Loomis, S. Yerci, N. Miljkovic, G. Chen, *Nat. Commun.* **2014**, *5*, 4449.
[49] P. Hou, D. Li, N. Yang, J. Wan, C. Zhang, X. Zhang, H. Jiang, Q. Zhang, L. Gu, D. Wang, *Angew. Chem., Int. Ed.* **2021**, *60*, 6926.
[50] R. Niu, J. Ren, J. J. Koh, L. Chen, J. Gong, J. Qu, X. Xu, J. Azadmanjiri, J. Min, *Adv. Energy Mater.* **2023**, *13*, 2302451.
[51] Q. Xi, Y. Yang, X. Liu, W. Wang, X. Ai, H. Yang, G. Zhao, Y. Yang, M. Wu, K.-G. Zhou, *Sep. Purif. Technol.* **2024**, *343*, 127086.